RSC Advances

ROYAL SOCIETY
OF **CHEMISTRY**

PAPER

View Article Online
View Journal | View Issue

Cite this: *RSC Adv.*, 2020, **10**, 24697

Large interlayer spacing $Nb_4C_3T_x$ (MXene) promotes the ultrasensitive electrochemical detection of Pb^{2+} on glassy carbon electrodes†

P. Abdul Rasheed, [a] Ravi P. Pandey,[a] Tricia Gomez,[a] Michael Naguib[b] and Khaled A. Mahmoud *[a]

A $Nb_4C_3T_x$ (MXene)-modified glassy carbon electrode was used for the electrochemical detection of Pb^{2+} ions in aqueous media. The sensing platform was evaluated by anodic stripping analysis after optimizing the influencing factors such as pH, deposition potential, and time. The large interlayer spacing, high *c* lattice parameter and higher conductivity of $Nb_4C_3T_x$ compared to other MXenes enhance the electrochemical detection of Pb^{2+}. The developed sensor can reach a detection limit of 12 nM at a potential ~ -0.6 V. Additionally, the developed sensor showed promising selectivity in the presence of Cu^{2+} and Cd^{2+}, and stability for at least 5 cycles of continuous measurements with good repeatability. This work demonstrates the potential applications of $Nb_4C_3T_x$ towards the development of effective electrochemical sensors.

Received 16th May 2020
Accepted 18th June 2020

DOI: 10.1039/d0ra04377j

rsc.li/rsc-advances

Introduction

Lead (Pb) is a common heavy metal, used in a variety of industrial processes and anthropogenic activities.[1] Pb^{2+} ions are known for their extremely harmful biological toxicity through enzyme inhibition and induction of oxidative stress and can cause chronic damage to several human body systems, including kidneys, gastrointestinal system, nervous system, and reproductive system.[2–4] Moreover, Pb contamination poses a serious health and environmental hazard due to its high accumulation and low clearance rate at contaminated sites.[5,6] The maximum level of Pb^{2+} in drinking water set by the United States Environmental Protection Agency (EPA) is 15 $\mu g\ L^{-1}$ (72 nM),[7] while the World Health Organization (WHO) limit for the blood Pb^{2+} level is 100 $\mu g\ L^{-1}$ (483 nM).[5,8]

Various techniques are used for the detection of Pb^{2+} in water including atomic absorption/fluorescence spectrometry, optical emission spectrometry, inductively coupled plasma mass spectrometry, and chemical or optical sensors.[9–11] Despite their reliability, the operations and maintenance associated with these methods are tedious, costly, and not suitable for on-site monitoring. Electrochemical techniques are inexpensive, selective, highly sensitive and effective alternative for the detection of various toxic substances and heavy metals.[12–14] Moreover, electrochemical methods are characterized by their portability, easy operation, quick analysis time, and low maintenance and instrumentation costs.[8,15] Stripping voltammetry (especially anodic stripping) have been used as the sensitive and powerful electrochemical technique for the detection of heavy metal ions.[1,9] Different carbon nanomaterials such as carbon nanotubes, graphene, and its composite materials have been used as the sensing platform for sensitive Pb^{2+} detection.[16–20]

The 2D transition metal carbides and carbonitrides (MXenes) have attracted broad attention with unique physicochemical properties.[21–24] The large lateral size with few nanometer thickness, embedded with good hydrophilicity, and activated metallic hydroxide sites render MXenes as promising materials for environmental remediation applications.[25–28] MXene surfaces is negatively charged due to its surface functional groups, which facilitate the adsorption of several toxic heavy metals and emerging contaminants.[27,29] In addition, MXenes nanosheets having strong trapping power to small cations, due to less inter planner distance (<2 Å).[30] It was reported that $Ti_3C_2T_x$ which is the most studied MXene, is an efficient adsorbent for the gold, lead and chromium cations.[30] In addition, the intercalation of different cations with various sizes and charges are possible between $Ti_3C_2T_x$ layers.[30] After alkalization intercalation of $Ti_3C_2T_x$, alk-MXene ($Ti_3C_2(OH/ONa)_xF_{2-x}$) exhibits superior sorption behavior for Pb^{2+} in presence of high levels of interfering cations such as Ca^{2+} and Mg^{2+}.[31] Recently, alkalization-intercalated $Ti_3C_2T_x$ modified electrode displayed enhanced electrochemical response towards the detection of Cd^{2+}, Pb^{2+}, Cu^{2+} and Hg^{2+}.[32] The alkalization process increases the *c* lattice parameter of $Ti_3C_2T_x$

---

[a] *Qatar Environment and Energy Research Institute (QEERI), Hamad Bin Khalifa University (HBKU), Qatar Foundation, P. O. Box 34110, Doha, Qatar. E-mail: kmahmoud@hbku.edu.qa*

[b] *Department of Physics and Engineering Physics, Tulane University, New Orleans, LA, USA*

† Electronic supplementary information (ESI) available. See DOI: 10.1039/d0ra04377j

from 19.741 Å to 26.187 Å and the alkalization process results in unique morphology and alteration in surface chemistry. This leads to enhanced electrochemical responses for alkalization-intercalated $Ti_3C_2T_x$ towards the heavy metal detection in comparison with the $Ti_3C_2T_x$.

$Nb_4C_3T_x$ is another member of the MXenes family, prepared by etching of Al from the Nb_4AlC_3 MAX phase.[33,34] Recently, $Nb_4C_3T_x$ have been explored in a number of applications, including dye adsorption,[35] energy storage devices,[23,36–38] hematopoietic recovery,[33] photothermal tumor eradication,[22] supercapacitors,[39] and photocatalytic hydrogen production.[40] Even though, the electrochemical performance of $Nb_4C_3T_x$ has not been widely explored towards sensing applications.

In this paper, we evaluate the electrochemical performance of Nb_2CT_x and $Nb_4C_3T_x$ on the glassy carbon electrode (GCE) and their application as sensing platform for the detection of Pb^{2+} in the aqueous media. To the best of our knowledge, this is the first report discusses the application of $Nb_4C_3T_x$ as electrochemical sensor for heavy metals.

Experimental

Materials

Phosphate buffer (PB) solution, NaOH, H_2SO_4, $K_3[Fe(CN)_6]$, $K_4[Fe(CN)_6]\cdot 3H_2O$, sodium acetate, acetic acid, lead nitrate, copper sulfate and cadmium acetate were purchased from Sigma Aldrich. The MAX phases of Nb_2CT_x and $Nb_4C_3T_x$ (Nb_2AlC and Nb_4AlC_3 respectively) were prepared by mixing powders of niobium (Alfa Aesar, 99.98%, −325 mesh), aluminum (Alfa Aesar, 99.9%, −325 mesh), and carbon (Alfa Aesar, 99%, 7–11 micron) at different ratios, followed by heating under an argon (Ar) flow. The detailed procedure is given in the ESI† and in the ref. 34 and 37.

Synthesis of Nb_2CT_x and $Nb_4C_3T_x$

The synthesis of multilayered Nb_2CT_x (ML-Nb_2CT_x) and $Nb_4C_3T_x$ (ML-$Nb_4C_3T_x$) MXenes were done by hydrofluoric acid (HF) etching of Al layers from MAX phases Nb_2AlC and Nb_4AlC_3 respectively. The Nb_2AlC or Nb_4AlC_3 powders were stirred for 96 h at 40 °C after immersing in 50% HF aqueous solution. The resulting reaction mixture were washed 5 to 6 times using DI water and centrifuged at 3500 rpm to separate the ML-MXenes as settled powders from the supernatants. The resulting ML-MXenes were washed using ethanol, and dried at 30 °C under flow of argon. The delaminated Nb_2CT_x (DL-Nb_2CT_x) and $Nb_4C_3T_x$ MXenes (DL-$Nb_4C_3T_x$) flakes were prepared by probe sonication (Cole Parmer, Ultrasonic Processor, 60% amplitude, 750 watt) of ML-Nb_2CT_x and ML-$Nb_4C_3T_x$ MXenes (100 mg) in 5 mL of degassed DI water at 20 °C, under a flow of Ar gas for 1 h, followed by freeze-drying.

Characterization

The morphology of prepared DL-Nb_2CT_x and DL-$Nb_4C_3T_x$ MXenes were characterized by scanning electron microscopy (SEM), using a FEI Quanta 650 FEG. The transmission electronic microscopy (TEM) was performed by using FEI Talos F200×. The ethanol dispersions of DL-Nb_2CT_x and DL-$Nb_4C_3T_x$ were mounted on a lacey Formvar carbon-coated Cu grid for TEM analysis. Bruker D8 Advance X-ray diffractometer with Cu-Kα radiation (λ = 1.54056 Å) was used to record X-ray diffractograms.

Fabrication of DL-Nb_2CT_x and DL-$Nb_4C_3T_x$ modified electrodes and electrochemical analysis

Prior to experiments, GCE was polished with alumina powder followed by sonication in a copious amount of ethanol and distilled water. 0.2 mg of Nb_2CT_x/$Nb_4C_3T_x$ was dissolved in 1 mL of distilled water and homogeneous suspension was made by sonication for 1 min. Then, 6 μL of this suspension was deposited onto GCE and dried at room temperature for overnight under inert atmosphere. CHI760E electrochemical work station (CHI, Texas, USA) was used to conduct all electrochemical measurements with a three electrode system. The three electrode system consist of a modified GCE as the working electrode, Pt wire as the counter electrode, and Ag/AgCl in saturated KCl as the reference electrode. Cyclic voltammetry (CV) were performed at a scan rate of 100 mV s^{-1} in the 0.1 M PB solution (pH 7) and in the solution of 0.1 M KCl with 10 mM $[Fe(CN)_6]^{3-/4-}$. Electrochemical impedance spectroscopy (EIS) measurements were performed at a potential of 10 mV in the 100 kHz to 0.1 Hz frequency range.

Stripping voltammetry analysis

Square wave anodic stripping voltammetry (SWASV) measurements were used to detect Pb^{2+} in acetate buffer solution (0.1 M, pH 5.0) containing different concentration Pb^{2+}. The pre concentration step was performed at −1.2 V for 150 s while stirring the electrolyte solution. SWASV voltammograms were recorded after an equilibration period of 15 s, in the potential range from −0.8 V to 0 V with square wave potential scan having 4 mV increment potential, 25 mV amplitude and 50 Hz frequency. After each anodic stripping measurement, a desorption step was performed at a potential of 0.8 V for 100 s under stirring to remove the residual heavy metal ions on the electrode surface. For interference measurements, the pre concentration step was carried out at the potential of −1.2 V for 150 s while string the electrolyte solution containing Cd^{2+} and Cu^{2+} (5 times concentration than Pb^{2+}) followed by recording SWASV voltammograms in the potential range from −1.2 V to 0 V. Error bars shows the standard deviation for three repetitive measurements in each experiment.

Results and discussion

Material characterization

DL-Nb_2CT_x and DL-$Nb_4C_3T_x$ MXenes nanosheets were prepared by acid etching of Al layer using HF aqueous solution from their corresponding MAX phases as described in the Experimental section, followed by sonication and freeze drying. SEM images in (Fig. 1(a and c)) describe the typical accordion-like structure in both multi-layered (ML)-Nb_2CT_x and ML-$Nb_4C_3T_x$ (Fig. 1(a and c)). After probe sonication, DL-Nb_2CT_x and DL-$Nb_4C_3T_x$

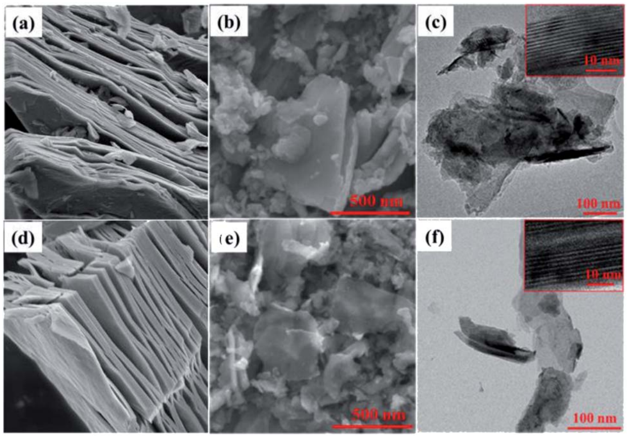

Fig. 1 SEM image of (a) ML-Nb_2CT_x (b) DL-Nb_2CT_x (d) ML-$Nb_4C_3T_x$ and (e) DL-$Nb_4C_3T_x$. TEM image of (c) DL-Nb_2CT_x and (f) DL-$Nb_4C_3T_x$. HR-TEM image of DL-Nb_2CT_x and DL-$Nb_4C_3T_x$ are shown in the inset of (c) and (f) respectively.

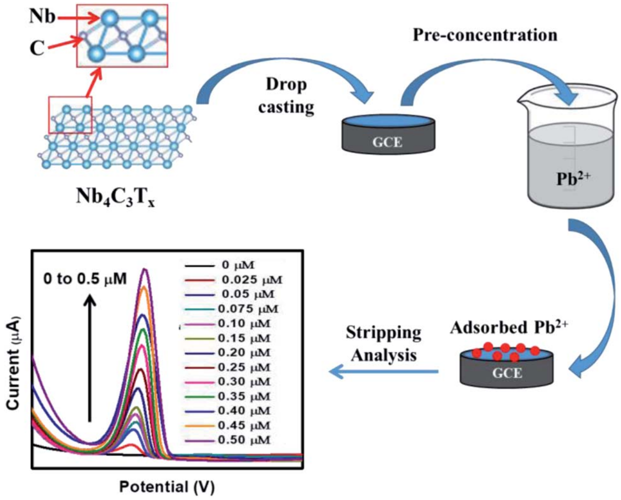

Scheme 1 The electrode fabrication and development of $Nb_4C_3T_x$ modified sensor for Pb^{2+} detection.

showed similar wrinkled sheet-like structure (Fig. 1(b and d)). Energy-dispersive spectroscopy (EDS) confirmed the presence of fluorine, oxygen, carbon and niobium elements in both MXenes (Fig. S1†). The TEM images revealed electron transparent single or few sheets with an average of 200–400 nm sheet size (Fig. 1(c and f)). In addition, the high resolution TEM (HR-TEM) images of DL-Nb_2CT_x and DL-$Nb_4C_3T_x$ shown in the inset shows the *d*-spacing ~11.5 Å and ~15 Å, respectively.[36] The XRD patterns of ML-Nb_2CT_x, DL-Nb_2CT_x, ML-$Nb_4C_3T_x$ and DL-$Nb_4C_3T_x$ are given in Fig. S2.† After delamination the intensity of (002) peaks were increased while intensity of other peaks decreased. The strong characteristic peak (002) in both DL-Nb_2CT_x (at 2theta of 7.87°) and DL-$Nb_4C_3T_x$ (at 2theta of 5.94°) confirmed the successful delamination and preparation of DL-MXenes.[23,35] DL-Nb_2CT_x has a smaller *c* lattice parameter (c-LP) of 22.44 Å as compared to 29.70 Å for DL-$Nb_4C_3T_x$, as calculated from (002) peak position. The corresponding interlayer distance for DL-Nb_2CT_x was 11.22 Å and 14.85 Å for DL-$Nb_4C_3T_x$, which is in a good agreement with the TEM results. The interlayer spacing in DL-$Nb_4C_3T_x$ were higher than that of DL-Nb_2CT_x, which could explain the interplanar distance increases with carbide blocks (n) in each MXene layer of $M_{n+1}X_nT_x$. A 14.85 Å spacing of DL-$Nb_4C_3T_x$ is larger than most studied MXenes.[41] As far as the electrochemical performance is concerned, larger interlayer space allows faster adsorption and intercalation of ions, and it enhances ion diffusion and charge transport of the electrolyte.[42]

Electrochemical characterization of Nb_2CT_x and $Nb_4C_3T_x$

The fabrication of $Nb_4C_3T_x$ modified GCE and the development of $Nb_4C_3T_x$ modified sensor for Pb^{2+} detection is given in Scheme 1. CV and EIS analysis were used to investigate the electrochemical behaviour of Nb_2CT_x and $Nb_4C_3T_x$ modified electrodes in an aqueous solution containing ferrocyanide/ferricyanide redox couple solution. As observed in Fig. 2(a), well-defined redox peaks were observed for all the electrodes and these peaks can be attributed to the reversible redox behaviour of $[Fe(CN)_6]^{3-/4-}$. The ΔE_p values for Nb_2CT_x/GCE and $Nb_4C_3T_x$/GCE were 197 mV and 141 mV, respectively and the lowest ΔE_p value of $Nb_4C_3T_x$/GCE indicating highest electron transfer kinetics than Nb_2CT_x/GCE. In addition, the ΔI_p values for Nb_2CT_x/GCE and $Nb_4C_3T_x$/GCE were 114.51 mV and 110.10 mV respectively. The higher value of ΔI_p again confirmed the highest electron transfer kinetics of $Nb_4C_3T_x$/GCE than Nb_2CT_x/GCE. The electrochemical active surface area was calculated by using the Randles–Sevcik equation and it has a value of 0.574×10^{-3} cm^2 and 0.621×10^{-3} cm^2 for Nb_2CT_x and $Nb_4C_3T_x$ respectively (see ESI†).[43] The Nyquist plot for Nb_2CT_x/GCE and $Nb_4C_3T_x$/GCE is given in Fig. 2(b). The charge transfer resistance (R_{ct}) parameter was obtained after fitting the Nyquist plot and was used to evaluate the electron-transfer kinetics of the redox couple at the electrode interface.[44] The R_{ct} values obtained for Nb_2CT_x/GCE and $Nb_4C_3T_x$/GCE were (2142 ± 24) Ω and (1732 ± 19) Ω respectively by fitting with R(Q[RW]) Randles equivalent circuit. The resistivity is lowest for $Nb_4C_3T_x$/GCE and hence $Nb_4C_3T_x$ is having the highest conductivity than Nb_2CT_x which can be justified by the higher 'n' value of $Nb_4C_3T_x$ ($n = 3$) than Nb_2CT_x ($n = 1$).[45] From the CV and EIS analysis, it was found that $Nb_4C_3T_x$ having highest electrochemical activity.

Stripping behaviour of Pb^{2+} and optimization of experimental parameters

The SWASV response of the bare GCE, Nb_2CT_x/GCE and $Nb_4C_3T_x$/GCE were analyzed for the detection of Pb^{2+} ions using acetate buffer solution containing 0.5 μM Pb^{2+}. Compared with the bare GCE, well defined stripping peaks at around −0.58 V were observed for the Nb_2CT_x/GCE and $Nb_4C_3T_x$/GCE and the peak current is highest for $Nb_4C_3T_x$/GCE than Nb_2CT_x/GCE (Fig. 3(a)). The highest response for $Nb_4C_3T_x$ can be attributed to large interlayer spacing, high *c* lattice parameter value than Nb_2CT_x which is evident from TEM and XRD measurements. In addition, it was established that the resistivity of $Nb_4C_3T_x$ is

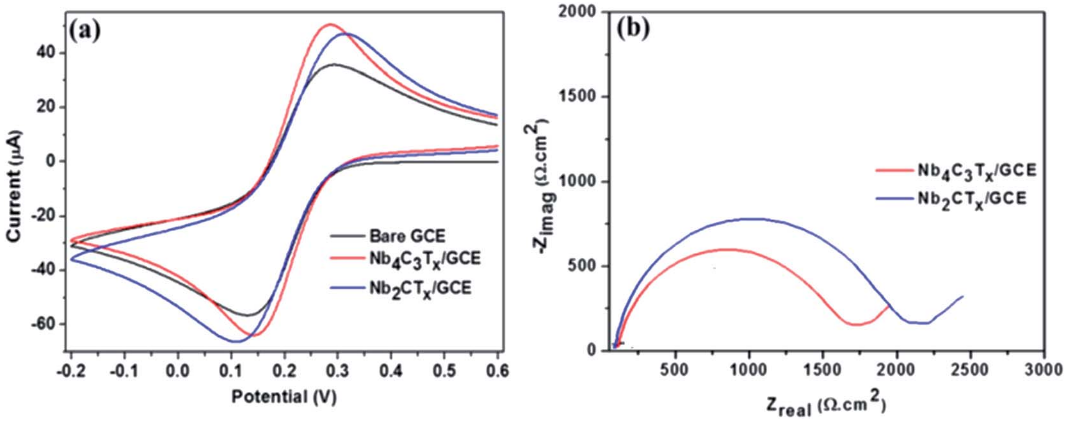

Fig. 2 (a) CVs of bare GCE, Nb_2CT_x/GCE and $Nb_4C_3T_x$/GCE. (b) Nyquist plots of Nb_2CT_x/GCE and $Nb_4C_3T_x$/GCE. Frequency range: 0.1 Hz to 10 kHz. The experiments were performed in the solution of 0.1 M KCl with 10 mM $[Fe(CN)_6]^{3-/4-}$.

lower than Nb_2CT_x,[45] which corresponds to the higher conductivity of $Nb_4C_3T_x$ as evident from electrochemical analysis (Fig. 2). Hence, $Nb_4C_3T_x$ has been selected as the sensing platform for the sensitive detection of Pb^{2+}.

The optimum conditions for highly sensitive Pb^{2+} detection were evaluated by changing the critical parameters such as pH, deposition time and potential. The impact of pH on the stripping current was studied from 3.0 to 6.0 (Fig. 3(b)). The peak current of Pb^{2+} was increased with increasing the pH from 3.0 to 5.0 and then decreased at pH = 6. The presence of [Nb–O]–H$^+$ groups favours the ion exchange behaviour of $Nb_4C_3T_x$ and this behaviour increases with the pH which results in the

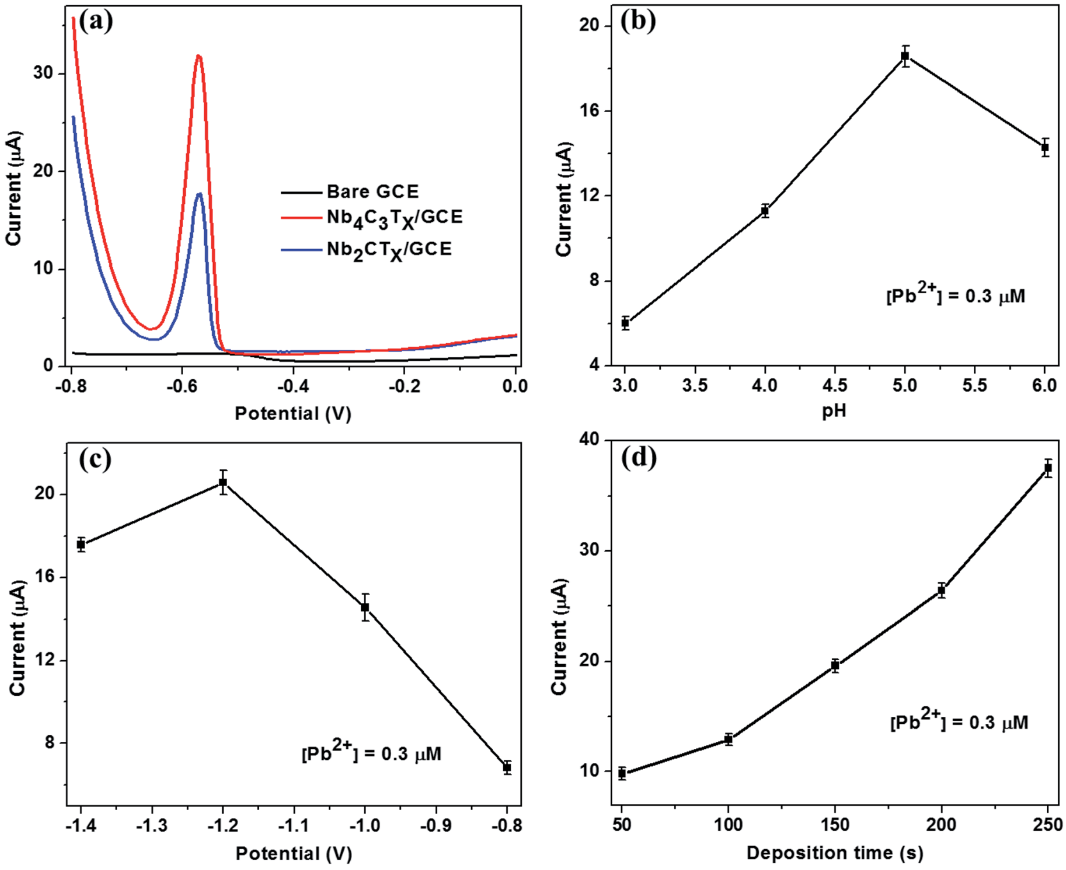

Fig. 3 (a) SWASV responses for bare GCE, Nb_2CT_x/GCE and $Nb_4C_3T_x$/GCE in presence of 0.5 μM of Pb^{2+} in 0.5 M acetate buffer at pH 5, deposition potential of −1.2 V and deposition time of 150 s. Optimization of experimental parameters. (b) pH, (c) deposition potential, and (d) deposition time towards the stripping current of $Nb_4C_3T_x$/GCE.

strengthening of stripping current.[32] The decrease in peak currents at pH 6 could be attributed to the hydrolysis of cations results in the formation of more $Pb(OH)_2$, which inhibits the further accumulation of Pb^{2+}. Considering the maximum observed stripping peak current, pH 5 was selected as optimal for subsequent experiments.

Deposition potential and time are also critical factors for stripping analysis to detect heavy metal ions. The deposition potential was varied from −1.4 to −0.8 V and the resulting stripping currents increases with negative potential until −1.2 V (Fig. 3(c)). A reduction in the current response was observed at deposition potential lower than −1.2 V. This might be due to occurrence of more hydrogen evolution in the acetate buffer. Hence, the deposition potential of −1.2 V was selected as optimal for further experiments. The deposition time was varied from 50 to 250 s and the stripping peak currents response was evaluated (Fig. 3(d)). The stripping peak current have increased linearly with the deposition time increase. A deposition time of 150 s was selected for subsequent experiments considering the concession between short measurement time, high sensitivity and good reproducibility favoured for practical applications.

Quantitative detection of Pb^{2+}

Under the optimal conditions, the quantitative detection of Pb^{2+} was performed by SWASV on $Nb_4C_3T_x$/GCE. Fig. 4(a) shows the SWASV responses at different concentrations from 0 to 0.5 μM of Pb^{2+}. The stripping peak currents increases with increasing the Pb^{2+} concentration and a good linear relationship was observed in the concentration range from 0.025 μM to 0.5 μM. There was no response for the developed sensor when the Pb^{2+} concentration was less than 0.025 μM and this concentration can be regarded as limit of quantification of the sensor. The corresponding calibration plot is given in Fig. 4(b), by plotting the peak current *vs.* Pb^{2+} concentration. The calibration plot equation was represented as i (μA) = 58.49[Pb^{2+}] + 1.13, with 0.99688 as correlation coefficient (R^2). The limit of detection (LOD) was calculated as 12 nM (S/N = 3), which is much lower (or comparable) than the similar kind of sensors for Pb^{2+} detection (refer Table 1). In a similar work with alkaline intercalated $Ti_3C_2T_x$ MXene as platform for electrochemical detection of heavy metals, the stripping analysis showed a detection limit of 32 nM with linear range of 0.10–0.55 μM and this response is significantly higher than bare $Ti_3C_2T_x$. The analytical performance of $Nb_4C_3T_x$ modified GCE is higher compared to bare $Ti_3C_2T_x$ as well as alkaline intercalated $Ti_3C_2T_x$. The analytical performance of $Nb_4C_3T_x$ modified GCE was compared with other similar reported electrodes (summarized in Table 1) and it showed that the $Nb_4C_3T_x$ modified GCE exhibited a wider range, promising detection limit and enhanced sensitivity. The large interlayer spacing and high c lattice parameter of $Nb_4C_3T_x$ (in comparison with Nb_2CT_x) have allowed for the adsorption of larger amount of Pb^{2+} between the sheets as well as the higher conductivity of $Nb_4C_3T_x$ have improved the electrochemical response on the electrode surface. This strategy can be easily implemented into screen printed electrodes for practical and portable applications considering the versatile sensor fabrication by drop-casting $Nb_4C_3T_x$ on the electrode followed by drying.[46]

Selectivity, stability and repeatability

The selectivity of the $Nb_4C_3T_x$/GCE was analyzed in the presence of Cu^{2+} and Cd^{2+} as inferring agents in 5 fold excess along with Pb^{2+} ion. The SWASV was performed under the optimum conditions. It is found that no or negligible change in the peak current of Pb^{2+} in presence of interfering ions. The peak for Cu^{2+} at around −0.1 V,[32] is present in the SWASV curve as shown in Fig. 5(a). The peak for Cd^{2+} at around −0.8 V,[32] is not clearly visible; however, the current response is higher in the particular range where the peak for Cd^{2+} normally visible. Fig. 5(b) shows the current response for the individual metal ions (Pb^{2+}, Cd^{2+}, Cu^{2+}) and their mixture at −0.58 V. The peak current was almost the same for Pb^{2+} alone and in the mixture with other interfering ions. These is no current response at particular potential of −0.58 V for the electrolyte solution containing Cd^{2+} or Cu^{2+}. These results confirmed the insignificant impact of interfering

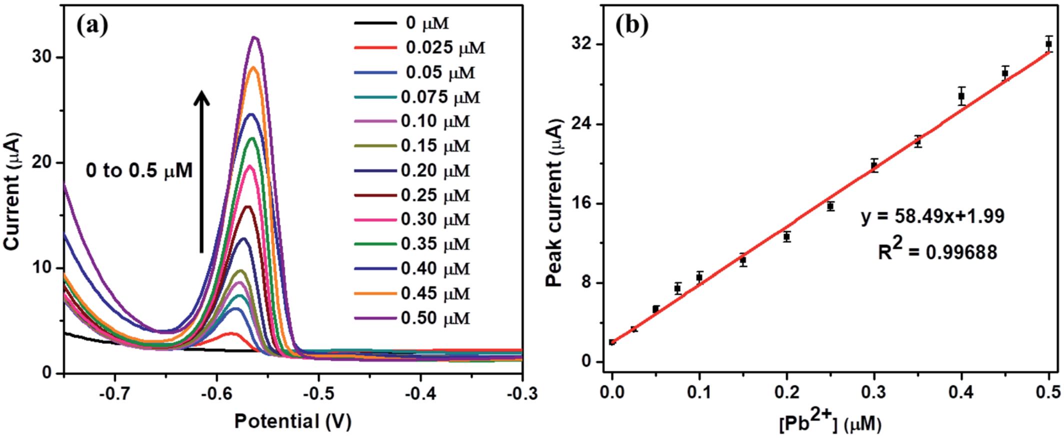

Fig. 4 (a) SWASV response of the $Nb_4C_3T_x$/GCE for in presence of Pb^{2+} from 0 to 0.5 μM. (b) The calibration plot of peak current *vs.* Pb^{2+} concentrations.

Table 1 The analytical performance of different 2D materials used for Pb^{2+} detection

Electrode	Detection technique	Detection limit	Linear range	Ref.
L-Cys/AuNPs/NG/GCE	SWV	56 nM	1–80 μM	1
Bismuth modified exfoliated graphite	SWASV	53 nM	1.0–250 μM	9
MWCNT/P1,5-DAN/Pt	SWASV	2.1 μM	4 to 150 μM	16
MWCNT/5-Br-PADAP/GCE	SWASV	100 nM	0.9 to 114.6 μM	17
G/PANI/PS nanoporous fiber/SPCE	SWASV	3.30 μM	10-500 μM	18
L-Cys-rGO/GCE	DPASV	215 nM	0.4 to 1.2 μM	19
Nafion/G/PANI nanocomposite/SPE	SWASV	100 nM	1–300 μM	20
Alk-Ti_3C_2/GCE	SWASV	32 nM	0.10–0.55 μM	32
$Nb_4C_3T_x$/GCE	SWASV	12 nM	0.025–0.5 μM	This work

metal ions and hence the selectivity of the sensor at around −0.58 V.

The stability of the $Nb_4C_3T_x$/GCE was investigated after 5 repetitive measurements using the same electrode and electrolyte containing 0.2 μM Pb^{2+}. After every measurement, a desorption step at a potential of 0.8 V was performed before the next electrodeposition steps. It is found that the SWASV response was highly reproducible with RSD value of 2.34 (Fig. 5(c)). In addition, the stripping current of $Nb_4C_3T_x$/GCE for Pb^{2+} was measured after keeping the electrode at 4 °C for one week and the stripping current obtained was 94.3% of the initial current with RSD of 3.15. These results confirmed the stability of the $Nb_4C_3T_x$/GCE electrode towards the detection of Pb^{2+}. The reproducibility analysis of the sensor was carried out by using five identical $Nb_4C_3T_x$/GCE electrodes for the detection of Pb^{2+} using similar procedures. The SWASV responses for five different electrodes with 0.2 μM Pb^{2+} showing good

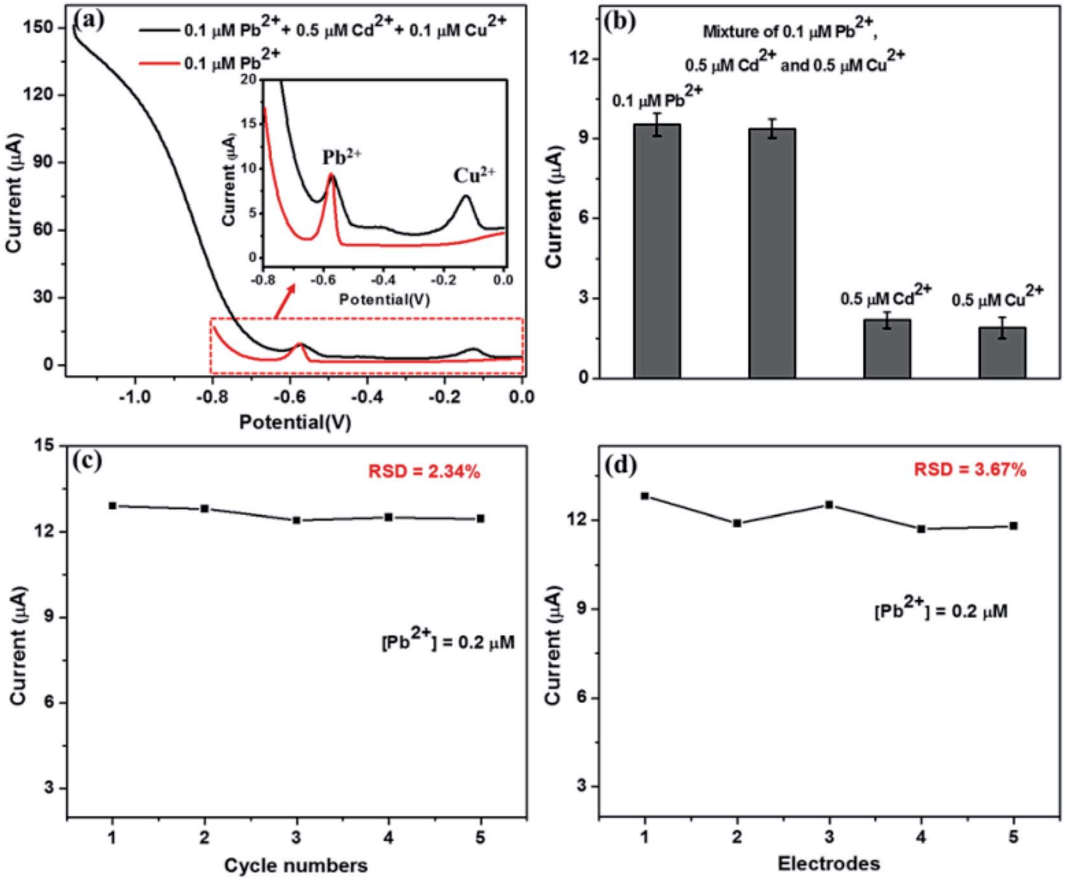

Fig. 5 (a) SWASV response of the $Nb_4C_3T_x$/GCE for Pb^{2+} (0.1 μM) in presence of Cd^{2+} (0.5 μM) and Cu^{2+} (0.5 μM). (b) Selectivity plot-SWASV response of the $Nb_4C_3T_x$/GCE at −0.6 V for different heavy metals. (c) The stability of $Nb_4C_3T_x$/GCE – SWASV responses for 5 repetitive cyclic measurements with 0.2 μM Pb^{2+}. (d) The repeatability of $Nb_4C_3T_x$/GCE – SWASV responses for 5 different electrodes with 0.2 μM Pb^{2+}.

Table 2 Recovery of Pb^{2+} in drinking water and tap water using the $Nb_4C_3T_x$/GCE sensor

Sample	Pb^{2+} added (μM)	Pb^{2+} detected (%)	RSD (%)
Drinking water (bottled)	0.05	95.8	2.35
	0.1	99.5	1.81
	0.2	96.5	2.57
Tap water	0.05	102.3	2.95
	0.1	97.5	3.02
	0.2	95.5	2.13

repeatability between different electrodes with RSD value of 3.67 (Fig. 5(d)).

Practical applications

To evaluate the practical applications of the developed $Nb_4C_3T_x$/GCE sensor, the response of the sensor has been measured after spiking the Pb^{2+} in bottled and tap water samples. The SWASV response of the sensor has been measured and the results are given in Table 2. The sensor exhibited a promising recovery between 95% and 102% with a relative standard deviation of 1.8–3.0%. From these results, it was confirmed that the developed sensor can be used for the detection of Pb^{2+} from samples.

Conclusions

The electrochemical behaviour of Nb_2CT_x and $Nb_4C_3T_x$ was investigated to explore its potential in electrochemical applications. The $Nb_4C_3T_x$ has demonstrated promising electrochemical performance and its electrochemical response is higher than Nb_2CT_x. The electrochemical detection capability of $Nb_4C_3T_x$ towards Pb^{2+} ions has been investigated by stripping analysis at optimized conditions. Evident by the high sensitivity and good reproducibility, the large interlayer spacing of $Nb_4C_3T_x$ can accommodate Pb^{2+} ions without destroying the layered structure of the electrode. The results showed that $Nb_4C_3T_x$ can be used as an immobilization platform for sensitive detection of Pb^{2+} with wide linear range and detection limit of 12 nM. This work validates the potential application of $Nb_4C_3T_x$ for the first time towards electrochemical sensing applications.

Conflicts of interest

There are no conflicts to declare.

Acknowledgements

PAR and RPP acknowledge the financial support from the National priority research program (NPRP) grants # NPRP8-286-2-118 and # NPRP9-254-2-120 from Qatar National Research Fund (A member of Qatar Foundation), respectively. Kaitlyn Prenger at Tulane University is acknowledged for the synthesis of MXenes used in this study. The authors acknowledge M. Pasha, A. R Shetty, and J. Ponraj of Core Labs, QEERI for SEM, XRD and TEM analysis respectively.

References

1 Y.-m. Cheng, H.-b. Fa, W. Yin, C.-j. Hou, D.-q. Huo, F.-m. Liu, Y. Zhang and C. Chen, *J. Solid State Electrochem.*, 2015, **20**, 327–335.

2 F. Gao, C. Gao, S. He, Q. Wang and A. Wu, *Biosens. Bioelectron.*, 2016, **81**, 15–22.

3 T. Ndlovu, O. A. Arotiba, S. Sampath, R. W. Krause and B. B. Mamba, *J. Appl. Electrochem.*, 2011, **41**, 1389–1396.

4 M. B. Gumpu, S. Sethuraman, U. M. Krishnan and J. B. B. Rayappan, *Sens. Actuators, B*, 2015, **213**, 515–533.

5 P. Chooto, P. Wararatananurak and C. Innuphat, *ScienceAsia*, 2010, **36**, 150.

6 H. R. Vanaei, A. Eslami and A. Egbewande, *Int. J. Pressure Vessels Piping*, 2017, **149**, 43–54.

7 A. Bala, M. Pietrzak, Ł. Górski and E. Malinowska, *Electrochim. Acta*, 2015, **180**, 763–769.

8 L. Wang, Y. Wen, L. Li, X. Yang, N. Jia, W. Li, J. Meng, M. Duan, X. Sun and G. Liu, *Biosens. Bioelectron.*, 2018, **115**, 91–96.

9 P. J. Mafa, A. O. Idris, N. Mabuba and O. A. Arotiba, *Talanta*, 2016, **153**, 99–106.

10 B. Feng, R. Zhu, S. Xu, Y. Chen and J. Di, *RSC Adv.*, 2018, **8**, 4049–4056.

11 B. Wen, J. Xue, X. Zhou, Q. Wu, J. Nie, J. Xu and B. Du, *ACS Appl. Mater. Interfaces*, 2018, **10**, 25706–25716.

12 B. Bansod, T. Kumar, R. Thakur, S. Rana and I. Singh, *Biosens. Bioelectron.*, 2017, **94**, 443–455.

13 M. R. Saidur, A. R. A. Aziz and W. J. Basirun, *Biosens. Bioelectron.*, 2017, **90**, 125–139.

14 M. Li, H. Gou, I. Al-Ogaidi and N. Wu, *ACS Sustainable Chem. Eng.*, 2013, **1**, 713–723.

15 Y. Fang, B. Cui, J. Huang and L. Wang, *Sens. Actuators, B*, 2019, **284**, 414–420.

16 H. D. Vu, L.-H. Nguyen, T. D. Nguyen, H. B. Nguyen, T. L. Nguyen and D. L. Tran, *Ionics*, 2015, **21**, 571–578.

17 A. Salmanipour and M. A. Taher, *J. Solid State Electrochem.*, 2011, **15**, 2695–2702.

18 N. Promphet, P. Rattanarat, R. Rangkupan, O. Chailapakul and N. Rodthongkum, *Sens. Actuators, B*, 2015, **207**, 526–534.

19 S. Muralikrishna, K. Sureshkumar, T. S. Varley, D. H. Nagaraju and T. Ramakrishnappa, *Anal. Methods*, 2014, **6**, 8698–8705.

20 N. Ruecha, N. Rodthongkum, D. M. Cate, J. Volckens, O. Chailapakul and C. S. Henry, *Anal. Chim. Acta*, 2015, **874**, 40–48.

21 M. Naguib, V. N. Mochalin, M. W. Barsoum and Y. Gogotsi, *Adv. Mater.*, 2014, **26**, 992–1005.

22 H. Lin, S. Gao, C. Dai, Y. Chen and J. Shi, *J. Am. Chem. Soc.*, 2017, **139**, 16235–16247.

23 O. Mashtalir, M. R. Lukatskaya, M.-Q. Zhao, M. W. Barsoum and Y. Gogotsi, *Adv. Mater.*, 2015, **27**, 3501–3506.

24 K. Rasool, R. P. Pandey, P. A. Rasheed, S. Buczek, Y. Gogotsi and K. A. Mahmoud, *Mater. Today*, 2019, **30**, 80–102.

25 C. Tan, X. Cao, X.-J. Wu, Q. He, J. Yang, X. Zhang, J. Chen, W. Zhao, S. Han, G.-H. Nam, M. Sindoro and H. Zhang, *Chem. Rev.*, 2017, **117**, 6225–6331.

26 J. Zhu, E. Ha, G. Zhao, Y. Zhou, D. Huang, G. Yue, L. Hu, N. Sun, Y. Wang, L. Y. S. Lee, C. Xu, K.-Y. Wong, D. Astruc and P. Zhao, *Coord. Chem. Rev.*, 2017, **352**, 306–327.

27 A. Shahzad, K. Rasool, W. Miran, M. Nawaz, J. Jang, K. A. Mahmoud and D. S. Lee, *ACS Sustainable Chem. Eng.*, 2017, **5**, 11481–11488.

28 Y. Ying, Y. Liu, X. Wang, Y. Mao, W. Cao, P. Hu and X. Peng, *ACS Appl. Mater. Interfaces*, 2015, **7**, 1795–1803.

29 A. Shahzad, M. Nawaz, M. Moztahida, J. Jang, K. Tahir, J. Kim, Y. Lim, V. S. Vassiliadis, S. H. Woo and D. S. Lee, *Chem. Eng. J.*, 2019, **368**, 400–408.

30 C. E. Ren, K. B. Hatzell, M. Alhabeb, Z. Ling, K. A. Mahmoud and Y. Gogotsi, *J. Phys. Chem. Lett.*, 2015, **6**, 4026–4031.

31 Q. Peng, J. Guo, Q. Zhang, J. Xiang, B. Liu, A. Zhou, R. Liu and Y. Tian, *J. Am. Chem. Soc.*, 2014, **136**, 4113–4116.

32 X. Zhu, B. Liu, H. Hou, Z. Huang, K. M. Zeinu, L. Huang, X. Yuan, D. Guo, J. Hu and J. Yang, *Electrochim. Acta*, 2017, **248**, 46–57.

33 X. Ren, M. Huo, M. Wang, H. Lin, X. Zhang, J. Yin, Y. Chen and H. Chen, *ACS Nano*, 2019, **13**, 6438–6454.

34 J. Yang, M. Naguib, M. Ghidiu, L.-M. Pan, J. Gu, J. Nanda, J. Halim, Y. Gogotsi and M. W. Barsoum, *J. Am. Ceram. Soc.*, 2016, **99**, 660–666.

35 C. Peng, P. Wei, X. Chen, Y. Zhang, F. Zhu, Y. Cao, H. Wang, H. Yu and F. Peng, *Ceram. Int.*, 2018, **44**, 18886–18893.

36 S. Zhao, X. Meng, K. Zhu, F. Du, G. Chen, Y. Wei, Y. Gogotsi and Y. Gao, *Energy Storage Mater.*, 2017, **8**, 42–48.

37 M. Naguib, J. Halim, J. Lu, K. M. Cook, L. Hultman, Y. Gogotsi and M. W. Barsoum, *J. Am. Chem. Soc.*, 2013, **135**, 15966–15969.

38 C. Zhang, M. Beidaghi, M. Naguib, M. R. Lukatskaya, M.-Q. Zhao, B. Dyatkin, K. M. Cook, S. J. Kim, B. Eng, X. Xiao, D. Long, W. Qiao, B. Dunn and Y. Gogotsi, *Chem. Mater.*, 2016, **28**, 3937–3943.

39 Y. Xin and Y.-X. Yu, *Mater. Des.*, 2017, **130**, 512–520.

40 T. Su, R. Peng, Z. D. Hood, M. Naguib, I. N. Ivanov, J. K. Keum, Z. Qin, Z. Guo and Z. Wu, *ChemSusChem*, 2018, **11**, 688–699.

41 J. Pang, R. G. Mendes, A. Bachmatiuk, L. Zhao, H. Q. Ta, T. Gemming, H. Liu, Z. Liu and M. H. Rummeli, *Chem. Soc. Rev.*, 2019, **48**, 72–133.

42 S. Zhao, C. Chen, X. Zhao, X. Chu, F. Du, G. Chen, Y. Gogotsi, Y. Gao and Y. Dall'Agnese, *Adv. Funct. Mater.*, 2020, 2000815.

43 P. V. Sarma, C. S. Tiwary, S. Radhakrishnan, P. M. Ajayan and M. M. Shaijumon, *Nanoscale*, 2018, **10**, 9516–9524.

44 H. Bagheri, N. Pajooheshpour, A. Afkhami and H. Khoshsafar, *RSC Adv.*, 2016, **6**, 51135–51145.

45 M. Ghidiu, M. Naguib, C. Shi, O. Mashtalir, L. M. Pan, B. Zhang, J. Yang, Y. Gogotsi, S. J. L. Billinge and M. W. Barsoum, *Chem. Commun.*, 2014, **50**, 9517–9520.

46 P. A. Rasheed and N. Sandhyarani, *Sens. Actuators, B*, 2014, **204**, 777–782.